Geophysical Journal International

Horizontal polarization of ground motion in the Hayward fault zone at Fremont, California: Dominant fault-high-angle polarization and fault-induced cracks

Journal:	*Geophysical Journal International*
Manuscript ID:	Draft
Manuscript Type:	Research Paper
Date Submitted by the Author:	n/a
Complete List of Authors:	pischiutta, marta; Istituto Nazionale di Geofisica e Vulcanologia - INGV Salvini, Francesco; Università Roma Tre, Dipartimento di Scienze Geologiche Fletcher, Joe; US Geological Survey rovelli, antonio; Istituto Nazionale di Geofisica e Vulcanologia - INGV Ben-Zion, Yehuda; University of Southern California, Department of Earth Sciences
Keywords:	Earthquake ground motions < SEISMOLOGY, Interface waves < SEISMOLOGY, Site effects < SEISMOLOGY, Wave propagation < SEISMOLOGY

Horizontal polarization of ground motion in the Hayward fault zone at Fremont, California: Dominant fault-high-angle polarization and fault-induced cracks

M. Pischiutta[1], F. Salvini[2], J. B. Fletcher[3], A. Rovelli[1] and Y. Ben Zion[4]

[1] Istituto Nazionale di Geofisica e Vulcanologia (INGV), Roma
[2] Dipartimento di Scienze Geologiche, Università Roma Tre
[3]US Geological Survey, Menlo Park, CA, USA
[4] Department of Earth Sciences, University of Southern California, Los Angeles, CA 90089-0740, USA

Abstract

We investigate shear-wave polarization in the Hayward fault zone near Niles Canyon, Fremont, CA. Waveforms of 12 earthquakes recorded by a seven-accelerometer seismic array around the fault are analyzed to clarify directional site effects in the fault damage zone. The analysis is performed in the frequency domain through H/V spectral ratios with horizontal components rotated from 0 to 180°, and in the time domain using the eigenvectors and eigenvalues of the covariance matrix method employing three component seismograms. The near-fault ground motion tends to be polarized in the horizontal plane. At two on-fault stations where the local strike is N160°, ground motion polarization is oriented N88°±19° and N83°±32°, respectively. At third on-fault station the motion is more complex with horizontal polarization varying in different frequency bands. However, a polarization of N86°±7°, similar to the results at the other two on-fault stations, is found in the frequency band 6-8 Hz. The predominantly fault-normal polarized motion at the Hayward fault is consistent with similar results at the Parkfield section of the San Andreas fault and the Val d'Agri area (a Quaternary extensional basin) in Italy. Comparisons of the observed polarization directions in several cases with models of fracture orientation based on the fault movement indicate that the dominant horizontal polarization is near-orthogonal to the orientation of the expected predominant cracking direction. The results help to develop improved connections between fault mechanics and near-fault ground motion.

1. Introduction

Large fault zones contain belts of damaged rocks with high crack density and granular materials that extend over widths ranging from tens to hundreds of meters (Ben-Zion & Sammis 2003, and references therein). These damage zones have reduced elastic moduli that lead to amplification of seismic motion (e.g., Cormier and Spudich, 1984; Li & Vidale, 1996; Calderoni *et al.*, 2010). Low velocity fault zone layers having sufficiently coherent geometrical and material properties over length scales of several km or more produce trapped waves that result from constructive interference of critically reflected phases (Ben-Zion and Aki, 1990; Li & Leary, 1990; Li *et al.*, 1997; Ben-Zion 1998).

Trapped waves with considerable motion amplification have been observed along many active faults (e.g., Ben Zion *et al.*, 2003; Peng *et al.*, 2003; Mizuno *et al.*, 2004; Lewis et al 2005), as well as in dormant fault damage zones (Rovelli *et al.*, 2002; Cultrera *et al.*, 2003). The basic form of trapped waves is Love-type with particle motion parallel to the fault zone layer (i.e. fault-parallel and vertical). However, small changes in the fault zone geometry can produce converted SV and P phases with particle motion normal to the fault. Examinations of large seismic data sets recorded by numerous fault zone stations indicate that while signatures of rock damage are abundant along faults, clear trapped waves are observed only in spatially-limited fault sections (e.g. Mamada *et al.*, 2004; Pitarka *et al.* 2006; Lewis and Ben-Zion, 2010).

In several recent studies polarization of shear waves near faults was found to be predominantly fault-normal. Rigano *et al.* (2008) observed in some faults of Mt. Etna (the Tremestieri, Pernicana, Moscarello and Acicatena faults) that seismic signals are strongly polarized and their orientation is never fault-parallel as would be expected for trapped waves. Using both volcanic tremor and local earthquakes, Falsaperla *et al.* (2010) found a strong polarization at seismological stations in the crater area of Mt. Etna, with polarization directions varying site by site but everywhere transversal to the orientation of the predominant local fracture field. Similarly, Di Giulio *et al.* (2009) found very stable polarization angles on Mt.

Etna, in the NE rift segment and in the Pernicana fault at Piano Pernicana, with horizontal polarization that again was never parallel to the fault strike. Di Giulio *et al.* (2009) ascribed the effect to local fault properties hypothesizing a role of stress-induced anisotropy and microfracture orientation in the near-surface lavas. Their basic idea was that, similarly to anisotropy along faults (Cochran *et al.,* 2003; Boness & Zoback, 2004; Peng & Ben-Zion, 2005), polarization might be dependent on the crack orientation in the shallow crust.

In the present paper we investigate ground motion polarization across the Hayward fault near Niles Canyon, Fremont, California. Using seismic records of seven accelerometer stations installed by the USGS since January 2008, we observe a tendency of on-fault stations to be polarized in the horizontal plane. This polarization in the region surrounding the fault shows a high angle in relation with the fault strike. Numerical models of the fracture distribution in the fault damage zone indicate that the polarization direction is orthogonal to the expected fracture cleavage developed by the fault activity. The same orthogonal relation characterizes also other faults where ground motion polarization was investigated. The occurrence of a strong horizontal polarization may reflect reduced elastic stiffness in the fault-normal direction.

2. Geological setting

The Hayward fault belongs to the San Andreas system that separates the Pacific plate and the Sierra Nevada microplate, accommodating 75-80% (38–40 mm/year) of the present relative motion between Pacific and North American plates (e.g., Argus & Gordon, 2001, Wakabayashi *et al.*, 2004), with a total dextral displacement of around 600 km. The San Andreas system is composed of a set of major dextral strike-slip faults, whose activity and distribution has irregularly shifted during the transform fault system history (Wakabayashi, 1999). Most faults show pull-apart basins and local transpressional structures related to step-overs and bends.

The Hayward fault exhibits a quite complex structure, with a general strike of N340°. It is predominantly a strike-slip right-lateral fault with about 100 km of offset during the past 12 Ma and at least a few hundred meters of east-up displacement over the past 2 Ma (Kelson and Simpson, 1995; Graymer *et al.*, 2002). The active surface trace of the Hayward fault is well documented from both geomorphic evidence and from the offset of man-made structures (Lienkaemper *et al.*, 1991), revealing that it is undergoing a significant creep (Savage and Lisowski, 1993; Lienkaemper, 1992) with some aseismic patches accommodating 50% or more of the long-term fault displacement. In spite of this, the fault has also experienced moderate to large earthquakes as the ~6.8 magnitude earthquake that occurred in 1868, whose rupture in surface was at least 30 km long or more (Lawson, 1908; Lienkaemper *et al*, 1991; Yu and Segall, 1996; Bakun, 1999). A Paleoseismic study performed in a trench on the Southern Hayward Fault (Fremont) by Williams *et al.* (1992) concluded that at least six ruptures on the Hayward Fault occurred during the past 2100 years.

The study area of the present work is located (Figure 1) in the southern sector of the fault in the Fremont district. Here the Hayward fault is largely aseismic and exhibits the highest surface creep rate (5 mm/yr) that is observed along the fault (Lienkaemper *et al.*, 1991). A seismic reflection profile across the creeping trace of the fault indicates that the fault dip is about 70° to the east in the 100 to 650 m depth range (Williams *et al.* (2005).

3. Data

In order to study ground motion polarization across the Hayward fault, we used data recorded by an array installed by researchers of the US Geological survey just across the fault near Niles Canyon, Fremont. The array was composed of seven stations equipped with K2 Kinematrics digitizer. Each accelerograph has a three-component set of accelerometers digitized at 200 sps. The stations were deployed in the backyards of single family homes and are shown in the inset of Figure 1 (colored labels) together with the surface creep trace of the fault (red line) traced by Lienkamper *et al.* (1991). The accelerographs were anchored to concrete and synchronized through a GPS receiver. The array recorded earthquakes since July 2008, including around 30 events between July 2008 and March 2009, whose hypocenters were taken from the Northern California Earthquake Data Center (http://quake.geo.berkeley.edu/). The epicenters were located along the San Andreas fault system, with source depths in the range 5-16 km. From the seismic events recorded by the accelerograph array, we selected 12 events with a high signal-to-noise ratio and with different focal mechanisms and source backazimuths ranging between N40W to N157E. The epicenters of these events are shown in Figure 1 with the projections of faults belonging to San Andreas system (cyan) and the array position (red triangle).

4. Analysis and results

The polarization analysis on the recorded seismic events was performed both in the time and in the frequency domains. The analysis in the frequency domain involved calculating the horizontal-to-vertical spectral ratios (HVSR) as a function of frequency and direction of motion, to investigate possible directional resonance effects and detect the frequency band where ground motion is mostly horizontal. The use of spectral ratios after rotation of the horizontal components was first introduced by Spudich *et al.* (1996), and subsequently exploited by Rigano *et al.* (2008) and Di Giulio *et al.* (2009) to detect horizontal polarization of ground motion in fault zones.

In this paper, HVSRs are calculated at each station separately for each event. We analyzed a time window of length varying from 10 to 20 sec (depending on events magnitude), comprising the significant portions of recordings windowed by a Hannning taper. The spectra of horizontal motions were computed after rotating the NS and EW components by steps of 10°, from 0° to 180°. Amplitude spectra of the vertical and horizontal components were also smoothed with a running mean filter with a width of 0.5 Hz.

The mean HVSRs averaged over the 12 selected events are shown in Figure 2. The stations are divided as “on-fault” if they are within tens of meters from the surface trace of the fault trace and “off-fault” if they are more than hundred meter from the surface trace. In the upper panels, the eighteen spectral ratios for different rotation angles (from 0° to 180°) are shown for each station, while the lower panels represent contour plots versus frequency and direction of motion. The on- and off-fault stations do not differ significantly in the HVSR amplitude levels. For all stations, horizontal motions tend to exceed the vertical ones in the approximate frequency band 1-7 Hz by about factor of 3, on the average. Examining the top panels for on-faults stations (right column) suggests that the spectral ratio amplitudes at peaked frequencies show a distinct variation as a function of the rotation angle. However, a similar feature is also evident at ND4 station which is at about 400 meters from the fault trace. In a quantitative comparison between on-fault and off-fault stations it is difficult to infer a difference between their polarization tendency using spectral ratios of Figure 2.

In order to better quantify the horizontal polarization of stations, the covariance matrix method (Kanasewich, 1981) was applied in the time domain. In this approach, a direct estimate of the polarization angle is achieved by calculating the eigen values of the covariance matrix using the three-component data (Jurkevics, 1988). The method solves the principal values which are interpreted to be the dominant polarizations. The results are used to estimate the angle between the geographic north and the projection of the largest eigenvector on the horizontal plane (see Appendix 1). The instantaneous polarization angle is estimated over 20% overlapping 0.5s running windows of the seismic records, after bandpass filtering the data between 1 and 7 Hz according to their spectral content (Figure 2).

The covariance matrix is calculated separately in each window with the basic assumption that each window shows only one dominant (or null) polarization. This assumes motions that are purely polarized over the window duration. The eigenvalues and eigenvectors are found by solving the algebraic eigen problem: they are real and positive, since the covariance matrix is positive and semidefinite, and they respectively correspond to the axis length and to the axis orientation of the polarization ellipsoid that describe the particle motion in the data window.

Compared to the previous applications of Rigano *et al.* (2008), Di Giulio *et al.* (2009) and Falsaperla *et al.* (2010), we use a hierarchical criterion to give a larger weight to time windows associated with more horizontal polarization ellipsoids and with a preferred and marked elongation. Details of the procedure are described in the Appendix 1.

The obtained results on horizontal polarization are illustrated in Figure 3. For each station, the distribution of polarization angles of all the events are merged and plotted in the left panels as rose diagrams. In the right panels the same values are stacked and plotted versus time with zero time being the P wave arrival. The dots are shown with different colors depending on the hierarchical class (**WH**) associated to each polarization value (see Appendix 1). The smallest values (yellow) appear in the first part of signals: this indicates that in the P-wave window vertical motions predominate and horizontal polarizations are randomly distributed. The highest values of **WH** (purple to black) persist during the S and coda waves. As shown in Figure 4 below, the difference between P waves and later arrivals is even more evident in the analysis of individual events.

In the rose-diagrams of off-fault stations, the polarization angles are scattered with no clear prevailing direction (Figure 3). This is mostly evident at stations ND1, ND4, ND5. In contrast, the three on-fault stations ND3, ND6, and ND7 (right panel) show a better defined polarization direction in the horizontal plane which seems to be persistent independently of the earthquake mechanism, distance and azimuth. Stations ND6 and ND7 depict a polarization oriented in N83°±32° and N88°±19° directions, respectively. These are very stable and persistent features especially at ND7. The polarization at ND3 is oriented N146°±14°. However, Figures 4 and 5 indicate that polarization at this station varies as a function of frequency, and this feature is clearer when observing the events separately.

A detailed illustration of polarization results associated with one representative event (# 8 in Table1) is presented in Figure 4. In panel A) the array geometry as well as the epicenter location and distance from the array are shown. Stations are grouped as on-fault (panel C) and off-fault (panel D). For each station, the velocity waveforms are depicted at the top. No evident amplitude variations and differences between on-fault and off-fault stations are found in the time series.

The HVSRs calculated for each station, are shown in the bottom panels. The amplified frequency band is underlined through a red dotted square. For on-fault stations ND6 and ND7, this frequency band (approximately 5-7 Hz) corresponds to the band where a E-W-oriented polarization was identified on the averaged results of Figure 3. The pattern of ND3 is more complex and will be discussed later on. The covariance matrix analysis is also performed for each station after bandpass filtering of seismic signals in the amplified frequency bands. The resulting polarization azimuths are plotted versus time and through a rose diagram in the middle panels. At on-fault stations the polarization directions of Figure 4 are close to the ones obtained as average of the whole data set in Figure 3. In contrast, off-fault stations show polarization directions and amplified frequency bands that vary between stations. On these stations a different pattern of polarization is observed on each analyzed seismic event, leading to an isotropic distribution of azimuths when averaging the whole data set (see Figure 3).

In order to verify whether the observed polarization could be ascribed to a source effect, the source polarization was modeled for direct P and S waves using the software ISOSYN (Spudich & Xu, 2003). The source-expected polarization was calculated as a function of focal mechanism, station distance and source backazimuth. This computation was made for the five earthquakes indicated with purple labels in Figure 1 (#1,4,8,10,12). For none of them the modeled source polarization was clearly identified on the array seismograms. The source polarization modeled for P and S waves for event #8 is shown in pane B) of Figure 4. The observed polarization was never consistent with the source expectation, leading to the conclusion that it is caused by a path or site effect. In any case, while the polarization expected for P waves in the horizontal plane is well recognized in the recorded first arrivals of events with a satisfactory signal-to-noise ratio, the polarization expected for S waves was never found. Because the distance between stations is more than a factor of 10 smaller than the distance between the array and the seismic source, the source-expected directions are the same for all the stations.

An interesting behaviour is observed on the HVRSs of station ND3 that highlight two different amplified frequency bands. In Figure 5 the HVSRs of ND3 for representative event #8 (already used in Figure 4). The polarization distribution is bimodal corresponding to a peak between 1 and 5 Hz with H/V amplification up to a factor of 6, and a second peak in the frequency band 6-8 Hz with amplification up to a factor of 12.

To separate the two directional effects, the covariance matrix analysis was performed in these two frequency bands (middle panels) For each frequency band the polarization angles versus time are plotted together with the band-pass filtered signals (EW, NS and Z components from top to bottom). The polarization angles are also plotted as rose diagrams by applying the hierarchical criterion described in the Appendix 1. The percentage of time windows exceeding the hierarchical selection is indicated as well.

Similar analyses of events #4,5,9,10 at station ND3 confirm polarization directions that vary in the two frequency bands, consistently with results of Figure 5. The combined result of the polarization analysis performed in the frequency band 6-8 Hz on all these events (including #8) are depicted in the bottom panel of Figure 5 as two rose diagrams: the cyan diagram represents all time windows whereas the blue one is obtained by applying the hierarchical criterion.

5. Discussion

Quantifying and understanding the factors controlling horizontal ground motion amplification and dominant polarization in damaged fault zone materials is important for topics ranging from wave propagation in complex media to engineering seismology. Ben-Zion and Aki (1990) showed with analytical model calculations that a low velocity fault layer with realistic parameters can produce motion amplification over factor 10 near the fault zone. Cormier & Spudich (1984) and Spudich & Olsen (2001) found a large amplification for 0.6-1.0 Hz waves within ~1-2 km wide low-velocity zone around the rupture of the 1984 Morgan Hill earthquake. Seeber *et al.* (2000) and Peng and Ben-Zion (2006) documented a factor 5 amplification of acceleration in a station located in the rupture zone of the 1999 Izmit earthquake on the Karadere branch of the NAF with respect to nearby off-fault station. Calderoni *et al.* (2010) observed a large difference in amplification between earthquakes occurring inside and outside the Paganica-San Demetrio fault during the April 2009 L'Aquila earthquake sequences, central Italy. As noted in the introduction, classical trapped waves have motion polarities that are predominantly in the fault parallel and vertical directions (e.g. Ben-Zion, 1998). However, natural fault zone structures are generally sufficiently complex to produce mode conversions and/or replace the trapped waves with diffuse amplified wavefield. Indeed, numerous observations indicate that large motion near faults is often dominated by polarization in the fault-normal direction (e.g., Rigano *et al.* 2008; Di Giulio *et al.*, 2009, Falsaperla *et al.* 2010).

In the present work we performed detailed analyses of dominant polarization angles of seismic waves generated by local earthquakes and recorded at a small array of accelerometers near the Hayward fault (Figure 1). Similarly to previous seismological studies, the analysis demonstrates a predominant polarization direction of shear waves near the fault zone that is inconsistent with the fault strike direction. As discussed in the previous section, the observations cannot be ascribed to the seismic source. Since the possible influence of the seismic path was removed by averaging results of selected earthquakes coming from different azimuths, the dominant directions are likely to have a near-station origin. At off-fault stations deployed outside the fault damage zone, a somewhat scattered distribution of polarizations is observed. In contrast, near-fault stations installed close to the fault trace show a common and persistent polarization effect oriented in an average E-W direction, independently of earthquake backazimuth and distance. For station ND3, which is located relatively close to the fault, a variation is found between two frequency bands: in the range 1-4 Hz a polarization oriented in N146°±14° direction is observed, while in the range 5-8 Hz the polarization is oriented N86°±7° in agreement with other fault zone stations (ND6 and ND7). Therefore, the mean polarization at stations associated with the fault damage zone forms an angle of about 70° with the fault strike direction. The observation of an effect strictly localized in the damage fault zone lead us to hypothesize a role of fracture systems (i.e. cracks). To check this hypothesis, we combine below modeling and additional observational results from different study areas where fault zone seismic data are available.

The damage zone associated with the development of a fault is assumed to be characterized by brittle deformation on both sides of the fault, with lateral extent that could range up to 200 m (Caine, 1996). We note that large faults may include intense damage that is strongly asymmetric and may reflect preferred propagation direction of recent earthquake ruptures (e.g., Ben-Zion and Shi, 2005; Dor *et al.*, 2006, 2008). However, in the following we focus on roughly symmetric damage products that reflect the early development stages of faults. Such damage zones are characterized by the presence of cracks (i.e. fracture systems referred also as fracture cleavages or Riedel fracture systems) with a systematic orientation. They are produced by the interaction of the tectonic stress and the near-fault local stress field associated with friction and fractures during the fault activity (Riedel 1929, Harding 1951, Hobbs *et al.*, 1976). As a result, consistent and often very intense closely spaced fracture sets are generated. Individual fractures can reach up to several meters with spacing down to one tenth of their dimension.

5.1 Interpretation of results

Depending on the local stress tensor and the brittle rheology of the hosting rock (Mandl, 2000), four types of fractures can develop: i) extensional fracture; ii) synthetic faulting or cleavage (i.e. with movement consistent with the main fault kinematics); iii) antithetic faulting or cleavage (i.e. with movement sense opposite to that of the main fault; iv) pressure solution surfaces. Their orientation depends on the direction of the resulting stress localized around the fault. The stress component due to the fault motion (the so-called kinematic stress component) often exerts the major influence on the final fracture orientation. In such cases, the maximum and minimum principal stress axes form angles of ~45° with the fault plane consistent with the fault motion, and the intermediate stress lies on the fault plane normal to the fault slip vector. As a result, the fracturing (cleavage) developed along a fault creates a damage zone that is characterized by well oriented fracture systems. Extensional fractures will develop normal to the minimum compressional axis, forming an angle of ~45° from the fault plane. Synthetic cleavage will form an angle of ~15° from the fault plane as measured in the sense of the fault motion. Antithetic cleavage will form an angle of ~65° as measured in the same way. Pressure solution surfaces will develop at ~45° normal to the maximum principal stress axis. Depending on the stress and kinematic conditions, one (or more) of these fracture type will develop, because the development of one set inhibits the growth of the others in their vicinity, reducing the capability to accommodate the elastic stress field. Typically, in kinematic conditions (as in the San Andreas system accommodating the relative motion between adjacent blocks), the main fracture set that is expected to develop is the synthetic cleavage.

To interpret the observed dominant polarization directions, we computed the direction of the synthetic cleavages expected for the Hayward fault, using the package FRAP (Salvini, 1999). The basic aspects of the package are described in Appendix 2. In agreement with Williams *et al.* (2005), the fault segment was modeled as a 20x8 km^2 representative surface, with an average strike of N20°W, reaching 11.5 km depth and dipping 70° to East. No minor irregularities were added on the fault surface since the fault movement occurred over a large time scale. Although Graymer *et al.* (2005) showed that the Hayward fault separates very heterogeneous regions with different lithotypes, in this model the rock rheological parameters were chosen to be the same on the two sides of the fault. Rheological parameters were thus fixed as: density 2400 kg/m^3, cohesion 5MPs, Poisson ratio of 0.25, friction angle of 30°, stress drop coefficient 50% and shale content 10%. The movement of the Hayward fault was set to be right-lateral strike-slip with a total displacement of 100 km. It is worthwhile to notice that the local stress analysis we performed is independent of the amount of displacement. The used displacement is just indicative of the expected maximum displacement for a fault segment of the chosen size and its amount influence only the fracture intensity. According to several works performed in the area to define the orientation of tectonic stress principal axis (e.g. Provost and Houston, 2003), the axis of maximum compression σ_1 was set to be oriented N5° and the axis of minimum compression σ_3 was set to be at N95°. Both σ_1 and σ_3 were assumed at the horizontal plane and the intermediate axis σ_2 was set vertical. As previously explained, for the Hayward fault the applied stress conditions were chosen to enhance the kinematic component caused by the fault movement, reducing the influence of the regional stress field.

Panel a in Figure 6 shows a sketch of a map view with the regional stress field (red arrows), the right-lateral fault movement in N160° direction (black arrows) and the kinematic components of the local stress field (K_1 and K_3). The expected fracture systems (cleavages and extensional fractures) are also illustrated. The orientation of synthetic cleavage as a projection on the horizontal plane is represented in panel b as a rose diagram. To help developing a correlation with measured polarization, the combined results from the analysis of seismic data at stations ND6 and ND7 are also plotted as a rose diagram in panel c. Both circular histograms were fitted through a Gaussian curve, obtaining a mean direction of N91°±38° for polarization angle and a mean direction of N1.5°±4° for synthetic cleavages. A difference in angle of 89.5° between the mean polarization and expected synthetic cleavages is found, suggesting an orthogonal relation between horizontal polarization and orientation of the most probable fracture system. A consistent perpendicular relation between fractures strikes and polarization has been also found for two other fault zones, the Parkfield section of the San Andreas Fault (Pischiutta et al., 2010), and the Eastern Agri fault system (Pischiutta, 2010), where abundant polarization data are available. Detailed results from these studies will be published in a separate paper. Here we only show and discuss, for comparison with the results for the Hayward fault, the obtained mean horizontal polarization obtained in those two study cases in the middle and bottom panels of Figure 6.

Data of HRSN network operated by the Berkeley Seismological Laboratory in Parkfield area were analyzed in order to study the occurrence of polarization and its spatial distribution across the San Andreas fault. Figure 6 displays (panel f) the mean polarization of ~2000 earthquakes recorded in 2004 at the borehole station MMNB installed in the fault damage zone. We find a predominant polarization effect in N 88 ± 39.7°. In the investigated sector the San Andreas is oriented in N140° direction (sketch in panel d of Figure 6), with an oblique right-lateral kinematics having a compressive component as revealed by the presence of positive flower structures. The associated most probable modeled fracture fields are synthetic cleavages expected in the N171± 3.6 direction, as depicted in panel e of Figure 6. According to our results, the dominant polarization in the Parkfield section of the San Andreas fault is oriented at 83° to the mean direction of the most probable fracture system, thus well approximating perpendicularity.

The Val d'Agri basin is the other case study where near-perpendicular relation between polarization and fractures was found. This area is characterized by many fault systems, being also well known for oil exploration (Menardi Noguera & Rea, 2000; Maschio *et al.*, 2005; Improta & Bruno, 2007; Pastori *et al.*, 2009). Figure 6 shows the results (panel i) for one station located near the Eastern Agri normal fault system (Cello *et al.*, 2000, 2003; Barchi et al,. 2007). The polarization analysis was performed on several earthquakes and resulted in a mean polarization direction of N54°±12°. Similarly to the two previous case studies, in panel g the sketch representing the fault and its brittle deformation pattern is drawn, using in this case a vertical section. The fault strike (not shown) is along the NW-SE direction. The representation in a vertical section is required because, in a normal fault, all the expected fracture systems (cleavages, extensional fractures and pressure solution) have the same strike, only differing by the dip angle. To show their variations in dip they are plotted as a Schmidt lower hemisphere projection in the inset of panel g. The modeling for this case indicates (panel h) that the most probable fracture systems is synthetic cleavage with a mean expected orientation of N139°±4°. Thus, also for this fault zone a transversal relation between the horizontal polarization and fracture field strike is found.

The near-perpendicular relation between the dominant orientation of cracks and wave polarization can be explained by considering the effective rock stiffness in different directions. In intensely fractured rocks, possibly mixed with granular materials, the resistance to loadings is strongly anisotropic. The effective Young modulus normal to a highly damaged material is expected to be considerably lower than the moduli in the other directions. This is intuitive and consistent with recent theoretical and observational results. Griffith *et al.* (2009) numerically simulated uniaxial compression tests of models of fractured rock with assumed crack distribution taken from mapped fault zone rocks. The results indicated strong anisotropic reduction of the effective fault-normal Young modulus, or increasing compliance with increasing angle between the load and the main fractures direction. Burjanek *et al.* (2010) observed strong polarization effects on weak seismic events and ambient vibration recorded on the unstable rock slope above the village of Randa (Swiss Alps). They hypothesized a relation with parallel dipping faults associated to the slope instability. According to their model, the rock stiffness is anisotropically reduced by the presence of fractures and horizontal vibrations are more pronounced in the direction of deformation that is also perpendicular to fractures. Findings by Burjanek *et al.* (2010) are consistent with the results of the present study, where we demonstrate that the dominant direction off cracks in the fault damage zone may control the frequently observed dominant fault-normal polarization direction.

6. Conclusions

We observed a strong horizontal motion polarization on the Hayward fault within a limited area corresponding to the fault damage zone. This finding is consistent with observations at other fault zones, both in strike-slip and extensional tectonic environments (Parkfield section of the San Andreas fault and Val d'Agri extensional basin, southern Italy, respectively). Similar polarization effects are also documented in fault zones of Mt. Etna volcano in Italy. Modeling of the fracture fields induced by the elastic stress and fault friction indicates an orthogonal relation between the wave polarization azimuth and the predicted strike of the synthetic fracture cleavage in the fault damage zone. For the Hayward fault with N160° strike and right-lateral movement, the observed mean polarization is oriented N91° and the synthetic cleavage is N175°, confirming a substantially perpendicular relation. For the Parkfield section of the San Andreas fault, where the kinematics is right-lateral with a compressive component, the mean polarization observed at station MMNB is also near perpendicular to the expected synthetic cleavage. Similarly, in the Val d'Agri basin characterized by extensional tectonics, the observed polarization is essentially perpendicular to the likely fracture systems produced in the damage zone by the normal fault movement. The comparison between fault fracture numerical modeling and polarization direction reveals that fault-induced crack systems play a major role in controlling the stiffness anisotropy in the fault damage zone, which in turn is responsible for the observed polarization. The results demonstrate the utility of using seismic signals with the employed relatively-simple and inexpensive technique to explore the distribution of fracture systems in fault zone environments.

FIGURES

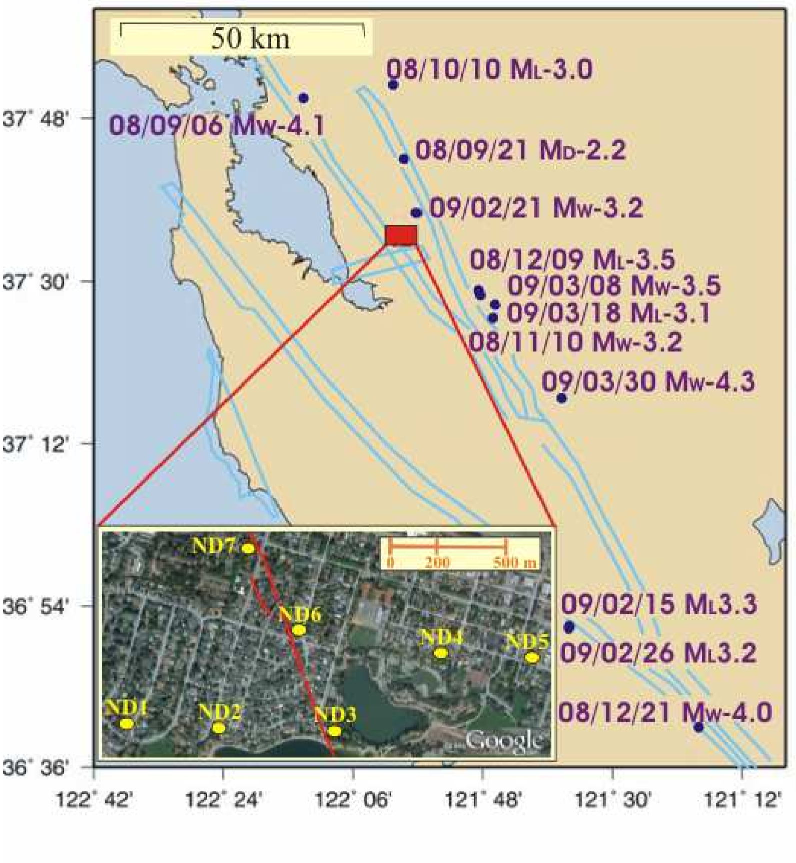

Figure 1 – Location of the accelerometric array area (red square). Cyan lines are the projection of the faults belonging to the San Andreas Fault System. Blue circles are the epicentres of the selected earthquakes with event date and estimated magnitude. The inset shows stations deployment near the Hayward fault trace at the surface as digitized by Lienkaemper et al., 2001 (red line).

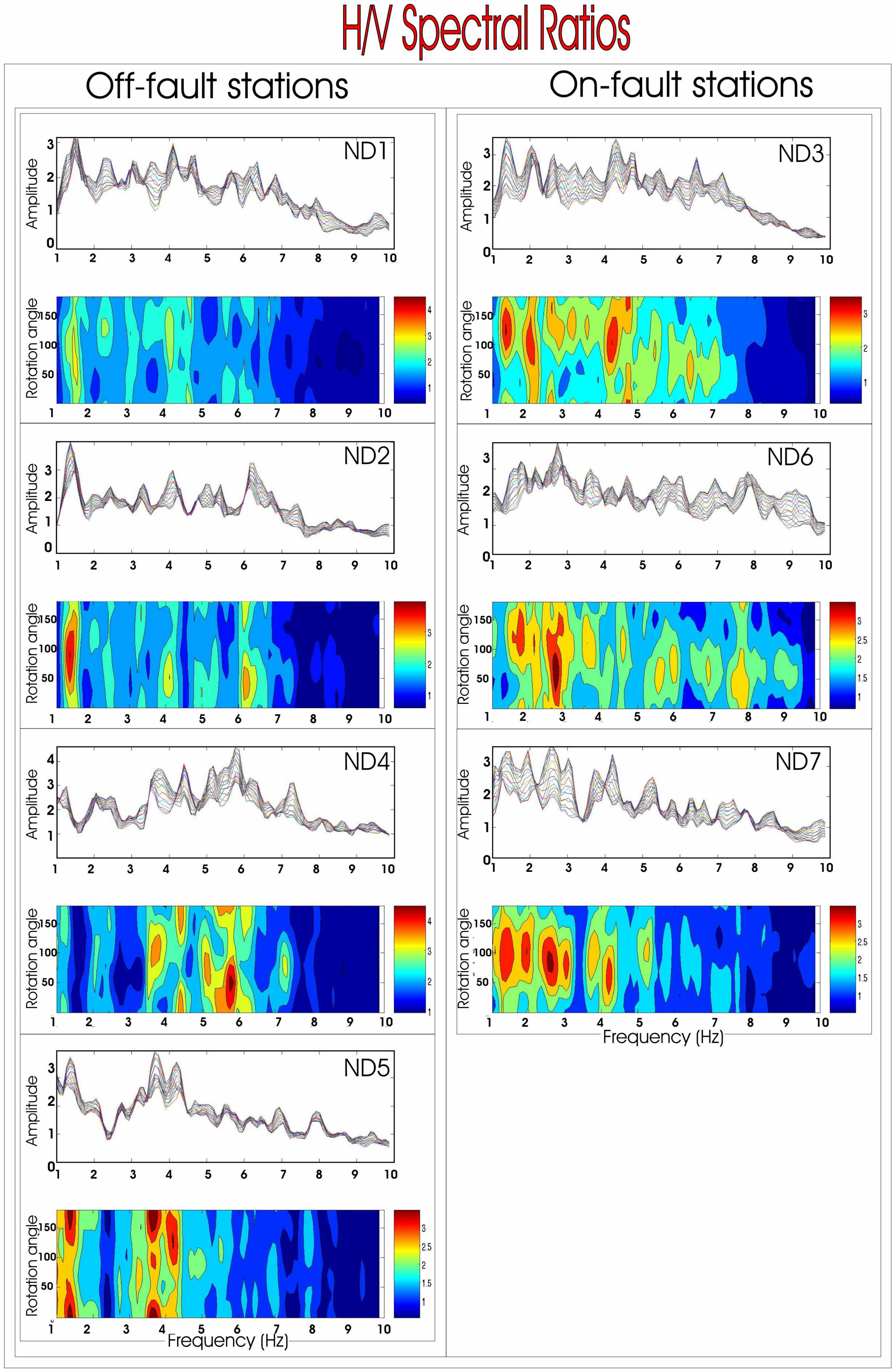

Figure 2 – Average horizontal-to-vertical spectral ratios of each accelerometric station. The geometric mean is computed over the ensemble of the 12 events selected. In the upper panels, average spectral ratios are drawn separately for rotation angle from 0° to 180°; in the bottom panels, the same spectral ratios are shown in a color contour representation.

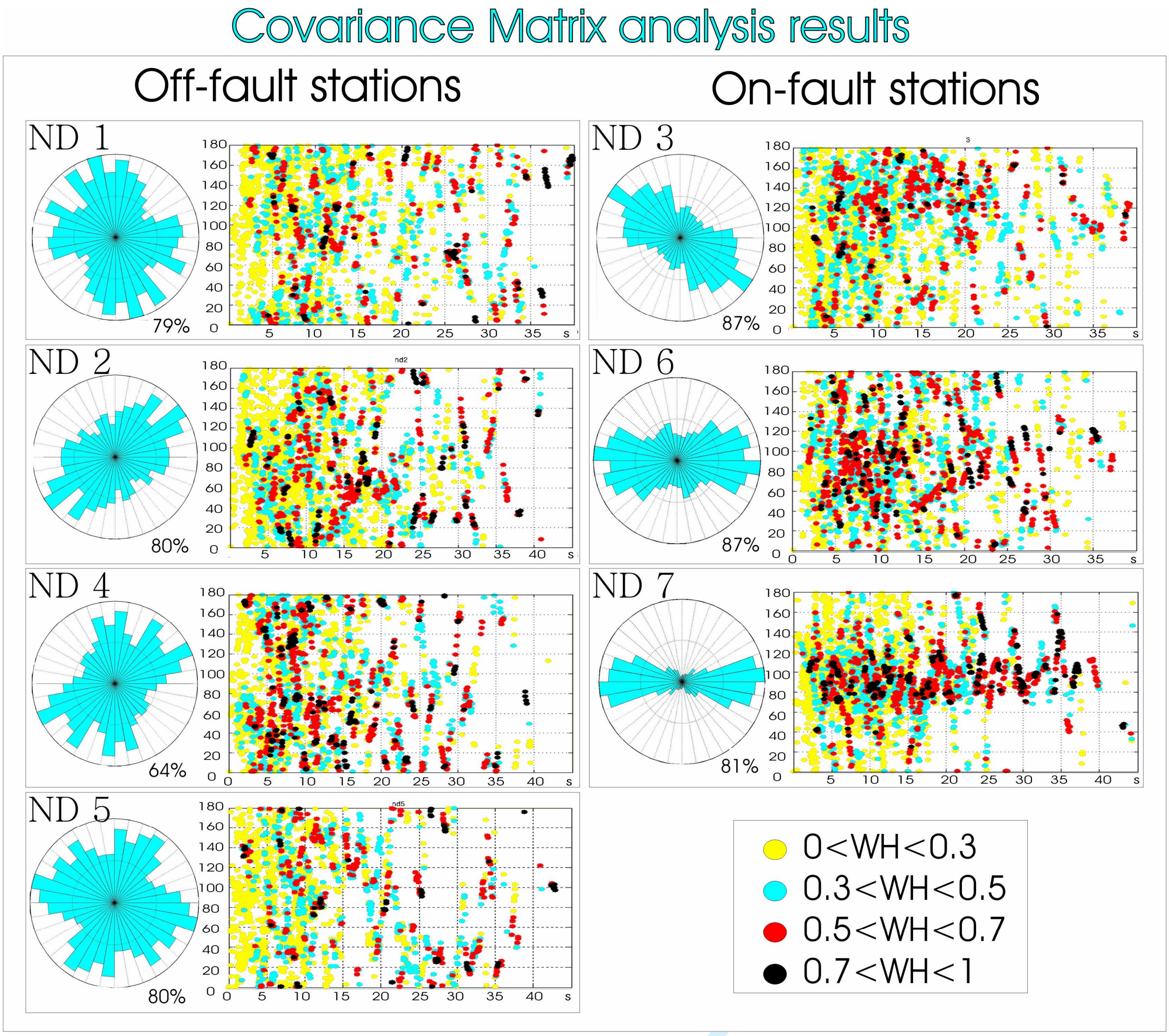

Figure 3 – Horizontal polarization angles computed from the covariance matrix analysis: for each accelerometric station, the results of the selected events are cumulated. The cumulated polarization angles are represented through rose diagrams (percentage at the bottom indicates the amount of time windows satisfying the hierarchical criterion) and are also plotted versus time, their color scale being related to the weight WH.

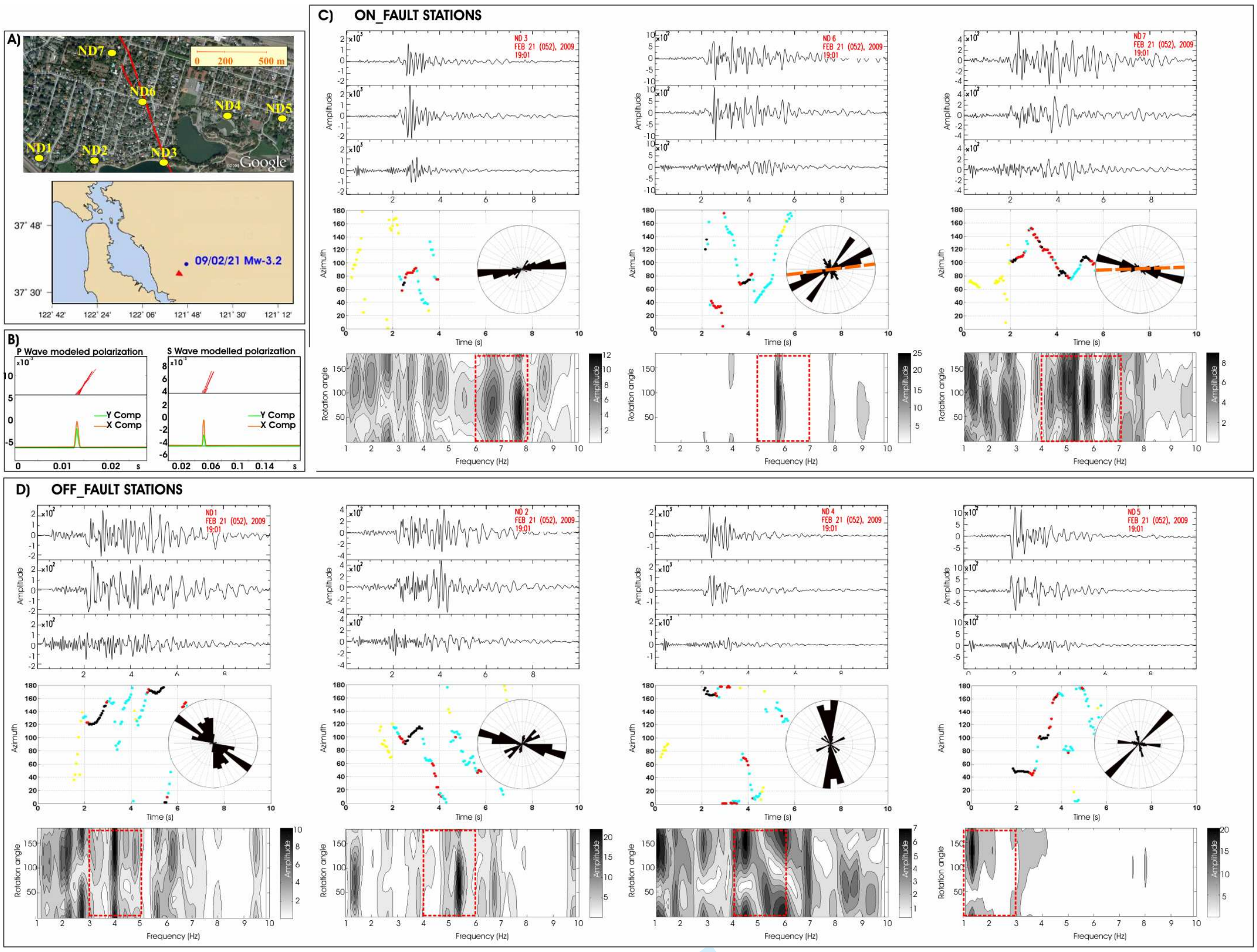

Figure 4 – Polarization analysis results for one representative event (#8 in Table 1). The array geometry with respect to the fault trace and the epicentre location are shown in panel (A). In panel (B) the source expected polarization for direct P and S waves is drawn. It was modeled using the software ISOSYN (Spudich & Xu, 2003) as a function of focal mechanism, station distance and source backazimuth. At the top of the two pictures, the expected polarization is depicted through red lines; the synthetic signals (N-S and E-W components) are shown at the bottom.
(Panel C and D) Horizontal polarization results of on-fault and off-fault stations, respectively. For each station, the HVSRs and the covariance matrix analysis results are drawn with the same modality of Figures 2 and 3 respectively. Time series are EW, NS and z components from the top to the bottom. The covariance matrix analysis was performed in the frequency band where HVSRs of each station are amplified. Resulting polarization values are plotted in middle insets both versus time and as rose diagrams. The selected frequency band is illustrated at each station through a dotted red square in the HVSRs contour graphs.

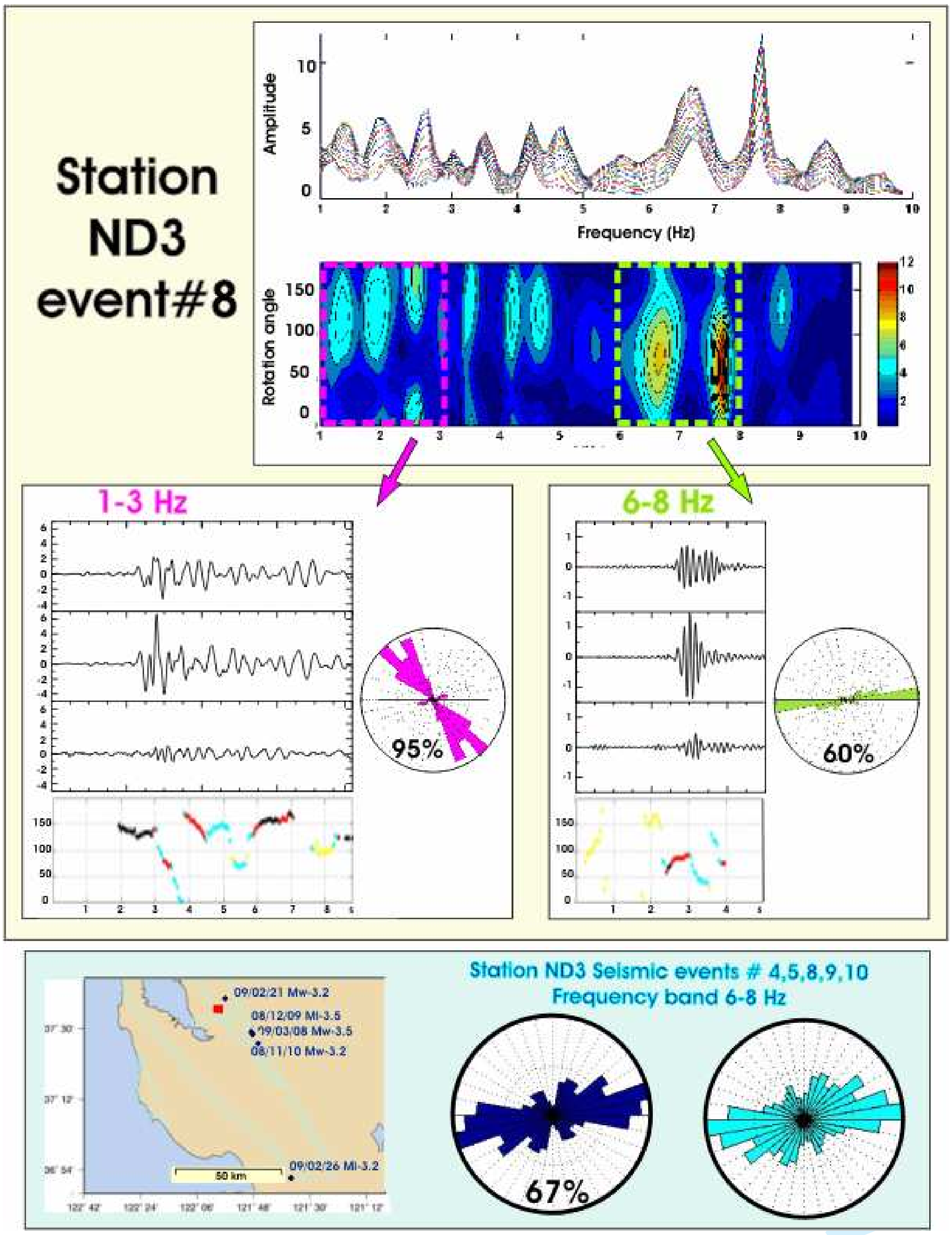

Figure 5 – Polarization analysis results at station ND3 for one representative event (# 8 of Table 1). **Top panel –** Horizontal-to-vertical spectral ratios of station ND3. Similarly to Figure 2, contour plot of amplitudes with rotation angle versus frequencies is shown at the bottom, while at the top the amplitude spectra of rotated components are plotted. **Middle panel -** Covariance matrix analysis results in the frequency bands 1-3 Hz (top) and 6-8 Hz (bottom) are depicted with the same modality of Figure 4. **Bottom panel -** Covariance matrix analysis cumulated results in the frequency range 6-8 Hz of events #4,5,9,10 at station ND3: the cyan diagram represents all time windows whereas the blue one is obtained by applying the hierarchical criterion (percentage of time windows exceeding the fixed thresholds is illustrated at the bottom). The inset shows the epicentral location of the selected events.

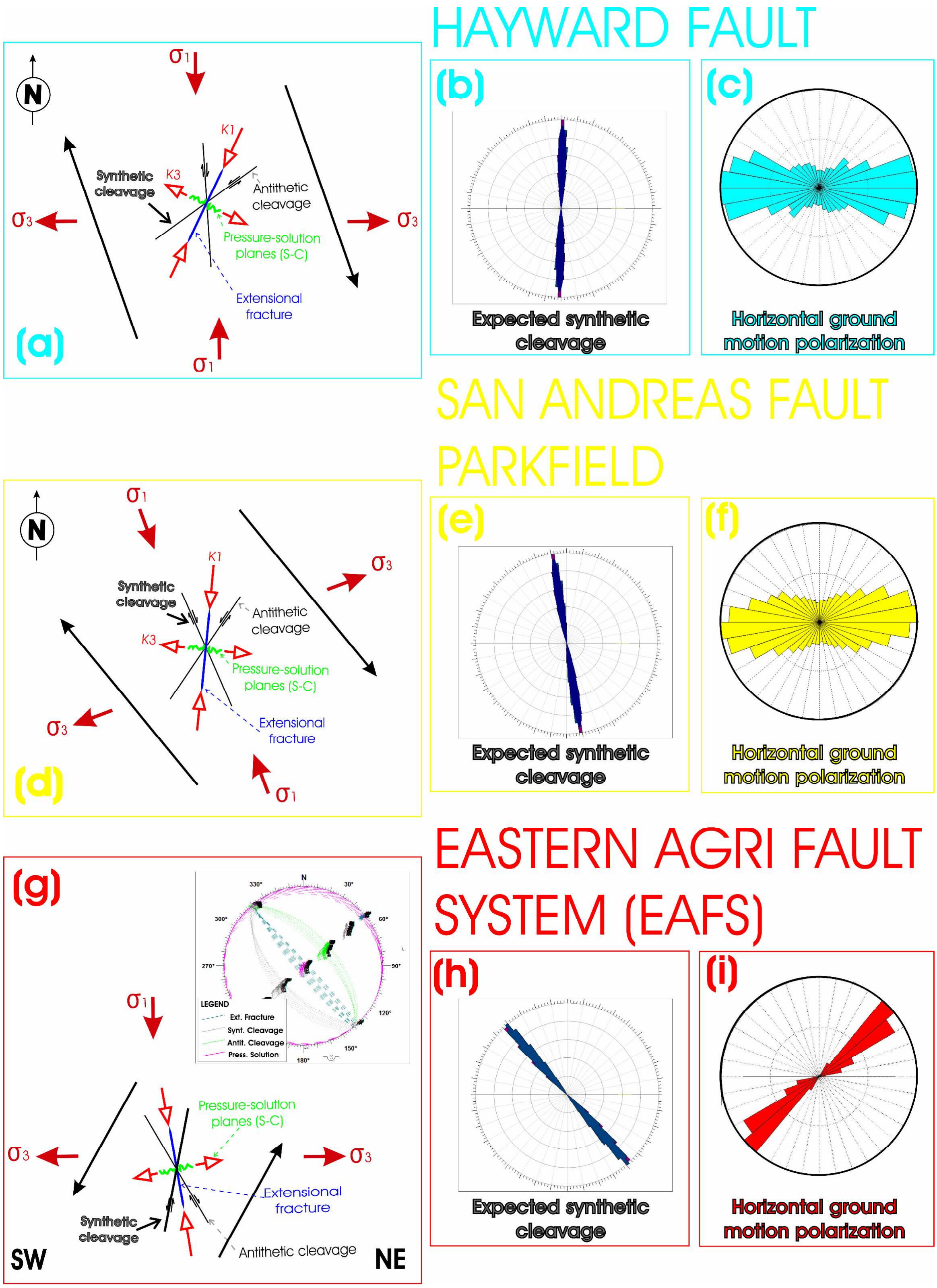

Figure 6 – TOP: Horizontal polarization across the Hayward fault. A Sketch in a map view is illustrated in **Panel a)** with the regional stress field (red arrows), the right-lateral fault movement in N160° direction (black arrows) and the kinematic components of the local stress field (K1 and K3). The expected fracture systems, as cleavages (black), extensional fractures (violet) and pressure solution (green) are also illustrated. The orientation of the most probable fracture field as a projection on the horizontal plane (synthetic cleavage) and modeled using the package FRAP 3 is represented in **Panel b)** as a rose diagram. To correlate theoretical trends with observed polarizations, results of stations ND6 and ND7 are cumulated and plotted as a rose diagram in **Panel c)**. MIDDLE: Polarization across the San Andreas fault in Parkfield sector where the fault strike is along N140° direction. The fault sketch in **panel d)** is drawn with the same structure of **Panel a)**. Similarly to the Hayward fault, the most probable fracture fields are synthetic cleavages, depicted in **Panel e)** through a rose diagram. The mean polarization of ~2000 earthquakes recorded in 2004 at the

borehole station MMNB installed in the fault damage zone is displayed in **Panel f**). BOTTOM: Polarization in the Val d'Agri extensional basin. A station close to one of the border dip-slip faults is selected. Similarly to the previous case studies, in **Panel g)** the sketch representing the fault and its brittle deformation pattern is drawn, in this case as a vertical section. The fault strike (not shown) is along the NW-SE direction. As expected for a normal fault, all the theoretical fracture systems (cleavages, extensional fractures and pressure solution) have the same strike and only differ by the dip angle. To show their variations in dip, they are plotted as a Schmidth lower hemisphere projection in the inset of **Panel g)**. The synthetic cleavage orientation modeled using the package FRAP 3 (Salvini, 1999), is depicted in **Panel h)** as a rose diagram. Results of the polarization analysis performed on several earthquakes are shown in **Panel i**).

TABLES

#	Day/hr/min	Lat.N	Long.E	Depth km	M	ND1	ND2	ND3	ND4	ND5	ND6	ND7
1	2008/09/06 04:00	37.8620	-122.0075	16.61	4.10 Mw	*	*	*	*	*	*	*
2	2008/09/21 16:20	37.7245	-121.9783	10.41	2.26 Md			*	*			
3	2008/10/10 23:19	37.8365	-122.2153	12.65	3.05 ML	*	*	*	*		*	*
4	2008/11/10 19:56	37.4335	-121.7750	10.02	3.20 Mw	*	*	*	*	*	*	*
5	2008/12/09 16:25	37.4835	-121.8095	6.13	3.49 ML	*	*	*	*	*	*	*
6	2008/12/21 17:35	36.6748	-121.3002	7.24	4.00 Mw	*	*	*	*	*	*	*
7	2009/02/15 22:05	36.8615	-121.5978	6.66	3.29 ML			*			*	
8	2009/02/21 19:01	37.6262	-121.9500	11.79	3.20 ML	*	*	*	*	*	*	*
9	2009/02/26 16:08	36.8627	-121.5997	6.70	3.24 ML		*	*				*
10	2009/03/08 14:47	37.4743	-121.8045	9.58	3.50 Mw	*	*	*	*	*	*	*
11	2009/03/18 02:26	37.4575	-121.7698	7.87	3.11 ML			*			*	
12	2009/03/30 17:40	37.2848	-121.6157	7.65	4.30 Mw	*	*	*	*	*	*	*

Table 1 – List of earthquakes selected for the analysis.

Appendix 1: Estimate of polarization angle through covariance matrix diagonalization

Spectral ratios using the rotated horizontal components are a powerful tool to recognize directional site effects (see Spudich et al., 1996; Cultrera et al., 2003). However, the spectral ratio may be biased by anomalies in the denominator spectrum. According to Jurkevics (1988), a direct estimate of the ground motion polarization can also be inferred using the covariance matrix.

In our implementation of this method, signals are detrended and the mean is removed, then they are bandpass filtered to restrict the analysis to the frequency band where HVRSs have previously revealed a significant (>2 at least) amplification. To diagonalize the covariance matrix, the code POLARSAC (La Rocca et al., 2004) is applied to the three components of motion in the time domain, using a partially overlapping moving window whose length is tailored depending on the predominant signal frequencies. After the matrix diagonalization, the eigenvalues $\lambda_1 \succ \lambda_2 \succ \lambda_3$ and eigenvectors $\vec{u}_i$ (i varying from 1 to 3) yield the axis length and orientation of the polarization ellipsoid in each time window.

The polarization vector is obtained from the vectorial sum:

$$PV = \sum_{i=1}^{3} \lambda_i \vec{u}_i \qquad \text{(A 1.1)}$$

It is defined through four parameters that characterize the polarization ellipsoid: AZ, I, R, and P. These parameters, inferred from the eigenvectors of each time window, are defined as follows.

AZ is the polarization azimuth measured as the angle between the geographic north and the projection of the main eigenvector on the horizontal plane:

$$AZ = \mathrm{arctg}\left[\frac{u_{21}(\mathrm{sign}\ u_{11})}{u_{31}(\mathrm{sign}\ u_{11})}\right] \qquad \text{(A 1.2)}$$

where u_{j1} j = 1 ,…, 3 are the three direction cosines of eigenvector $\vec{u}_1$. The sign function has been introduced to take positive vertical component of $\vec{u}_1$ resolving the 180° ambiguity (Jurkevics, 1988).

I is the apparent incidence angle, i.e. the angle between the eigenvector associated to the highest eigenvalue $\vec{u}_1$ and z-axis and is given by:

$$I = \arccos(u_{11}) \qquad \text{(A 1.3)}$$

R is rectilinearity, it ranges between 0 (spherical motion) and 1 (rectilinear motion) and indicates to what extent the three axes differ:

$$R = 1 - \frac{\lambda_2 + \lambda_3}{2\lambda_1} \qquad \text{(A 1.4)}$$

P is planarity, it ranges between 0 and 1, indicating to what extent the motion is confined to a plane:

$$P = 1 - \frac{2\lambda_3}{\lambda_1 + \lambda_2} \qquad \text{(A 1.5)}$$

Among these parameters, **AZ** is the one used to represent horizontal polarization in the present study. It is plotted through a circular histogram (rose diagram) computed from 0° to 360° at bins of 10°. Bins that differ by 180° are cumulated together as having the same polarization direction, their separation having no physical meaning. In order to increase the weight of AZ values of time windows with higher degree of rectilinearity and more horizontal motion, a hierarchical criterion is applied in the azimuth statistics.

The hierarchical criterion we establish excludes from the statistics values of AZ associated to $R < 0.5$ and $I < 45°$, semi-spherical or near-vertical polarization solutions being not relevant to our study. The other R and I values in the intervals $0.5 < R < 1$ and $45° < I < 90°$ are normalized linearly between 0 and 1. A weight factor WH is obtained from the product $WH = R*I$, where $0 < WH < 1$. The value of WH is used as a weight for the horizontal AZ values contributing to the rose diagrams of horizontal polarization.

To visually illustrate the highly restrictive selectivity of our hierarchical criterion, two time windows are shown as examples in Figure A1.1 where the corresponding results of I, R and AZ are visualized through the polarization ellipsoid. The weight factors calculated for the two time windows are shown as well.

The first time window (identified by an orange square) is characterized by a moderately high weight (WH=0.71) that is controlled by a high incidence (87°) and highly rectilinear ellipsoid (R=0.88). The second time window (identified by a blue square) is relative to a very small weight (WH=0.06), lower by more than one order of magnitude than the previous one. In this second case the ellipsoid still has a moderately high value of incidence (60°) and it is still quite rectilinear (R=0.59). Nevertheless the polarization azimuth of the first ellipsoid will give a much higher contribute to the construction of the final polarization histogram.

This hierarchical criterion is intentionally very restrictive, selecting only time windows with a high horizontal polarization degree, rejecting the others even though the polarization ellipsoid still is not so vertical and is elongated in a preferential direction.

To ensure that the statistics are representative of the whole time windows analyzed along the signals and that the hierarchical criterion did not lead to exclude too many samples, the percentage of rejected time windows is calculated and plotted near each rose diagram. Moreover, the values of AZ are plotted versus time and along signals to detect any changes with the different seismic phases. The associated weights are represented through a colour scale, as shown in Figure 3.

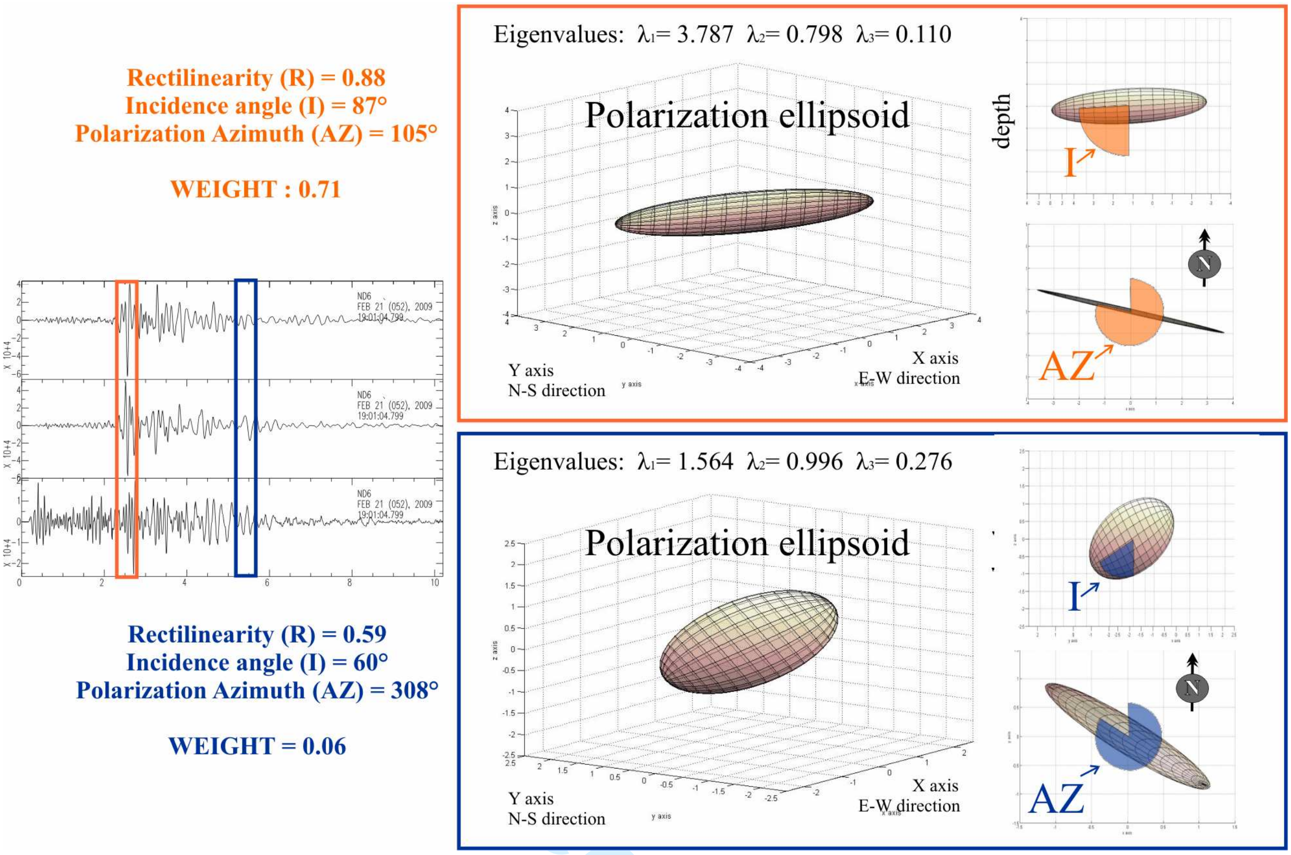

Figure A1.1 – Polarization analysis performed on two time windows to show the influence of incidence and rectilinearity values on the construction of the polarization ellipsoid. For each window the R, I and AZ values resulting from the covariance matrix analysis are reported as well as the calculated weight factors. Moreover the polarization ellipsoids are drawn on the basis of the eigenvalues obtained from the diagonalization of the covariance matrix, and the incidence and azimuth angles are represented on a vertical and plane section, respectively.

Appendix 2 – The Frap Package

The presence of faults results in the development of zones of local intense brittle deformations. Typically fault zones include an internal fault core, characterized by the presence of crushed and grinded material in complex pattern (Caine, 1996). Its dimension and amount of evolution of the grinding process are related to the stress conditions and the fault displacement. The fault core is surrounded by the fault damage zone, characterized by the presence of an organized set of brittle deformations and dilations. Again, its width and intensity of deformation are functions of the stress conditions, fault plane geometry and displacement occurring in the fault zone during fault activity.

The Frap Package is a tool that predicts the stress and brittle deformations in fault core and in the fault damage zones. It utilizes a combination of numeric and analytic approaches.

The fault is discretised into a grid of quadrangular cells, with each being characterized by an attitude and a position in a reference frame. For each cell, the various components of the stresses that acted though time are computed (Figure A2.1).

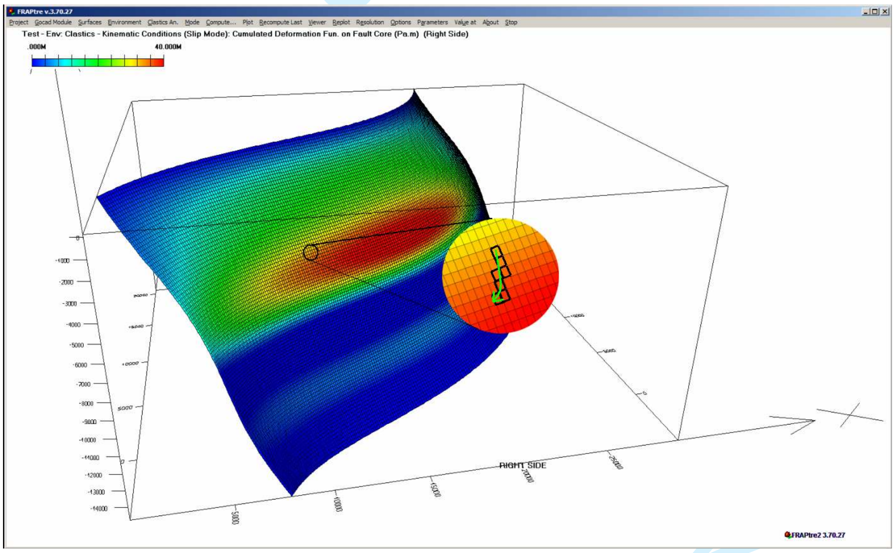

Figure A2.1 - Example of FRAP output showing the grid structure representing the fault zone. For each cell the stress/deformation components are analytically computed. The enlarged circle illustrates how to numerically compute the cumulative DF (or TSI, see text). The DF values of the cells falling on the displacement path of the cell are accumulated proportionally to the length of the path.

The model considers four stress components. The first one is the regional stress tensor, often responsible of the fault development, evolution and movement. This component can be introduced as a fixed value (as in the present study) or may be derived from a spatial distribution function.

The second tensor component is the overburden, that is the load of the material (e.g. rock, water) above the given cell. The vertical component is the σ_{1ov} and can be computed as:

$$\sigma_{1ov} = \int_{z_Q}^{z_S} (\rho(z) \cdot g) dz \qquad \text{(A 2.1)}$$

where z is depth, ρ is the density, g is the gravity acceleration.

The overburden stress conditions are assumed to be uniaxial, that is the two main horizontal components assume the same value as a function of the rock rheology at the cell:

$$\sigma_{2ov} = \sigma_{3ov} = \frac{\upsilon}{1-\upsilon} \cdot \sigma_{1ov} \qquad \text{(A 2.2)}$$

where υ is Poisson's ratio.

The third component is the fluid isotropic pressure within the rock pores, that obviously induces a decrease in the brittle strength of the rocks. It is computed from the height of the fluid column Hcol and-the fluid density ρ_F:

$$\mathrm{P} = \mathrm{Hcol} \cdot \rho_F \cdot g \qquad \text{(A 2.3)}$$

The stress variation due to the pore elasticity component is considered negligible.

The fourth component is referred in the package as the "kinematic stress" and is often the largest one in the fault zone. It is the component resulting from the brittle strain accumulation due to frictional resistance and failures associated with the fault.

This component can be described as a tensor oriented with the σ_{2k} main component lying on the cell surface normal to the movement vector on the cell, the σ_{1k} main component forms an angle of 45° from the surface compatible with the movement (see Fig. A2.2, panel a). The σ_{1k} module is equal to the strength of the fault surface to fail, computed according to the Coulomb-Navier Criterion (see below). The σ_{2k} represents the null axis and has a 0 value.

$$\sigma_{1k} = \Sigma$$

$$\sigma_{2k} = 0 \qquad \text{(A 2.4)}$$

$$\sigma_{3k} = -\Sigma$$

In this way, the resulting stress tensor on a cell will be the sum of all these components. The attitude of the kinematic stress tensor is a function of the cell surface attitude and the fault movement vector on the cell. Depending on the tectonic scenario, the kinematic component may be negligible, as in the case of no fault movement. In most cases, as in the fracture produced by the studied fault, it represents the most important stress component.

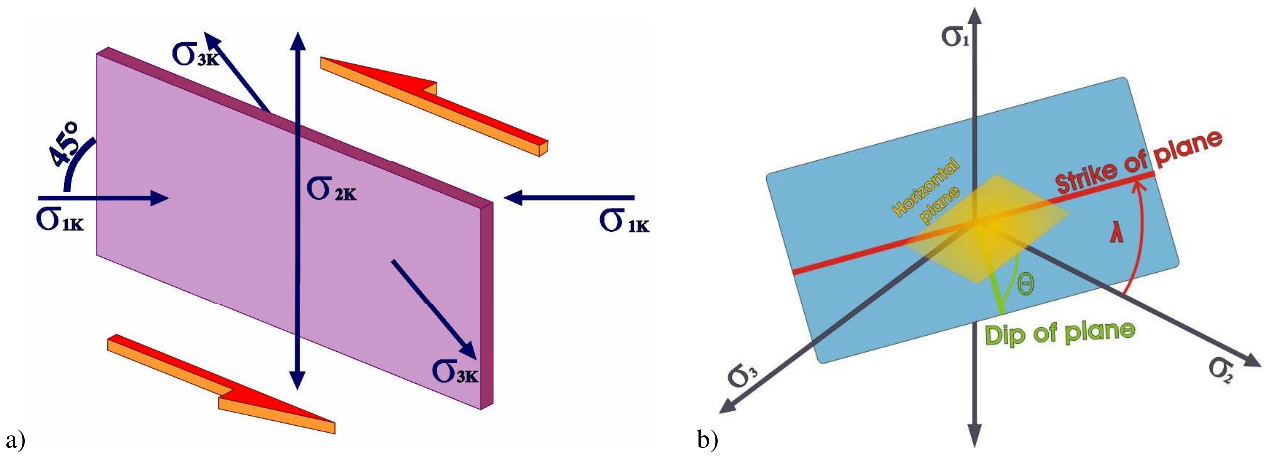

Figure A2.2 – Panel a) Fault surface (violet) and orientation of the kinematic stress components (blue arrows) related to the fault movement (red arrows) for a perfect fault (i.e. without transtension or transpression component). Panel b) Strike and dip values of the fault plane in the $\sigma_1\sigma_2\sigma_3$ reference system.

The resulting stress is then compared to the strength in the cell zone as predicted by available failure criteria. In the present study we choose the Coulomb-Navier Failure Criterion:

$$\Sigma = c + \tan\varphi(\sigma_N - P_w) \qquad \text{(A 2.5)}$$

Where σ_N is the stress component normal to the cell surface and is computed according to Jaeger et al. (2007) as follow:

$$\sigma_N = (\sigma_3 \cos^2 \lambda + \sigma_2 \sin^2 \lambda) \cdot \sin^2 \theta + \sigma_1 \cos^2 \theta \qquad \text{(A 2.6)}$$

λ and θ being respectively the azimuth and the dip of the fault surface with respect to the fault surface (see Figure A2.2 panel b).

The capability to produce fracture at each cell at a given time interval is represented by the deformation function D_f (Storti et al., 1997) that represents the difference between the strength Σ and the maximum shear τ^* acting on the cell surface (see Figure A2.2 panel b):

$$D_f = \tau^* - \Sigma \qquad \text{(A 2.7)}$$

Where, according to Jaeger at al. (2007), τ^* is given by :

$$\begin{aligned} \tau_s &= -0.5 \cdot (\sigma_3 - \sigma_2) \cdot \sin\theta \sin 2\theta \\ \tau_d &= 0.5 \cdot (\sigma_3 \cos^2 \lambda + \sigma_2 \sin^2 \lambda - \sigma_1) \cdot \sin 2\theta \\ \tau^* &= (\tau_d + \tau_s)^{\frac{1}{2}} \end{aligned} \qquad \text{(A 2.8)}$$

Thus from the resulting stress tensor at each cell is possible to compute the attitude of the different type of expected fracture sets (Riedel Fractures) as well as their probability to be produced from the statistic interpretation of the D_f.

The various type of brittle deformations (e.g., see Mandl, 2000) include: the synthetic cleavage (R Riedel planes), the antithetic cleavage (R' Riedel Planes), the extensional fractures (T Riedel Planes), and the pressure solution surfaces (P Riedel Planes). The term cleavage is used to describe a fracture set characterized by a spacing significantly shorter than the fracture dimensions.

The package then can compute the total brittle deformation for each cell through time along the trajectory that each cell follows along the fault during displacement (Fig. A2.1).

In the present application the use of the package was limited to compute the attitude of the main fractures that develop at each cell of the fault surface (i.e. synthetic fractures, R Riedel).

Finally, the resulting fracture field is output from the software and analyzed as structural elements by producing the rose diagrams shown in the article by the Daisy Package (Salvini et al., 1999), freely downloadable at http://host.uniroma3.it/progetti/fralab/.

REFERENCES

Argus, D. F. & Gordon, R. G., 2001. Present tectonic motion across the Coast Ranges and San Andreas fault system in central California. *Geol. Soc. Am. Bull.*, **113**, 1580– 1592.

Bakun, W. H., 1999. Seismic activity of the San Francisco Bay region. *Bull. Seismol. Soc. Am.*, **89**, 764–784.

Barchi, M., Amato, A., Cippitelli, G., Merlini, S. & Montone, P., 2007. Extensional tectonics and seismicity in the axial zone of the Southern Apennines. *Boll. Soc. Geol. It.*, Special Issue **7**, pp. 47–56.

Ben-Zion, Y., 1998. Properties of seismic fault zone waves and their utility for imaging low-valocity structures. *J. Geophys. Res.*, **103** (B6), 12567-12585.

Ben-Zion, Y. & Aki, K., 1990. Seismic radiation from an SH line source in a laterally heterogeneous planar fault zone, *Bull. seismol. Soc. Am.*, **80**, 971– 994.

Ben-Zion, Y., Peng, Z., Okaya, D., Seeber, L., Armbruster, J. G., Ozer, N., Michael, A. J., Baris, S. & Aktar, M., 2003. A shallow fault-zone structure illuminated by trapped waves in the Karadere-Duzce branch of the North Anatolian Fault, western Turkey, *Geophys. J. Int.,* **152**, 699 – 717.

Ben-Zion, Y. & Sammis, C. G., 2003. Characterization of Fault Zones . *Pure Appl. Geophys.,* **160**, 677-715.

Ben Zion, Y. & Shi, Z., 2005. Dynamic rupture on a material interface with spontaneous generation of plastic strain in the bulk. *Earth Planet. Sci. Lett.,* **236 (1-2)**, 486-496.

Boness, N. L. & Zoback, M. D., 2006. Mapping stress and structurally controlled crustal shear velocity anisotropy in California. *Geology*, **34(10)**, 825–828.

Burjanek, J., Gassner-Stamm, G., Poggi, V., Moore, J.R. & Fah, D., 2010. Ambient vibration analysis of an unstable mountain slope. *Geophys. J. Int.,* **180**, 820-828.

Caine, J.S., Evans, J. P. & Forster, C.B., 1996. Fault zone architecture and permeability structure. *Geology,* **24**,1025-1028

Calderoni G., Rovelli, A., Milana, G. & Valenzise, G., 2010. Do Strike-Slip Faults of Molise, Central–Southern Italy, Really Release a High Stress? *Bull. Seismol. Soc. Am.,* **100 (1)**, 307-324.

Cello, G., Gambini, R., Mazzoli, S., Read, A., Tondi, E. & Zucconi, V., 2000. Fault zone characteristics and scaling properties of the Val d'Agri fault system (Southern Apennines, Italy). *J. Geod.*, **29(3–5)**, 293– 307.

Cello, G., Tondi, E., Van Dijk, J.P., Mattioni, L., Micarelli L. & Pinti, S., 2003. Geometry, kinematics and scaling properties of faults and fractures as tools for modelling geofluid reservoirs; examples from the Apennines, Italy. *Geological Society, Special Publications*, **212,** 7–22.

Cochran, E. S., Li, Y.-G. & Vidale, J. E., 2006. Anisotropy in the shallow crust observed around

the San Andreas fault before and after the 2004 M 6.0 Parkfield earthquake. *Bull. Seismol. Soc.Am.*, **96**(4B), S364– S375, doi:10.1785/0120050804.
Cochran, E. S., Vidale, J. E. & Li, Y. -G., 2003. Near-fault anisotropy following the Hector Mine earthquake. *J. Geophys. Res.*, **108**(B9), 2436, doi:10.1029/2002JB002352.

Cormier, V. F. & Spudich, P., 1984. Amplification of Ground Motion and Waveform Complexities in Fault Zones: Examples from the San Andreas and Calaveras Faults. *G. J. Roy. Astr. Soc.* **79**, 35–152.

Cultrera, G., Rovelli, A., Mele, G., Azzara, R., Caserta, A. & Marra, F., 2003. Azimuth dependent amplification of weak and strong round motions within a fault zone (Nocera Umbra, Central Italy), *J. Geophys. Res.*, **108** (B3), 2156, doi:10.1029/2002JB001929.

Di Giulio, G., Cara, F., Rovelli, A., Lombardo, G. & Rigano, R., 2009. Evidences for strong directional resonances in intensely deformed zones of the Pernicana fault, Mount Etna, Italy. *J. Geophys. Res.*, **114**, doi:10.1029/2009JB006393.

Dor O., Ben-Zion, Y. Rockwell, T. K. & Brune, J., 2006. Pulverized Rocks in the Mojave section of the San Andreas Fault Zone. *Earth Planet. Sci. Lett.*, **245**, 642-654.

Dor O., Rockwell, T. K. & Ben-Zion, Y., 2006. Geologic observations of damage asymmetry in the structure of the San Jacinto, San Andreas and Punchbowl faults in southern California: A possible indicator for preferred rupture propagation direction, *Pure Appl. Geophys*., **163**, 301-349, DOI 10.1007/s00024-005-0023-9.

Dor, O., Yildirim, C., Rockwell, T.K., Ben-Zion, Y., Emre, O., Sisk, M. & Duman, T. Y., 2008. Geologic and geomorphologic asymmetry across the rupture zones of the 1943 and 1944 earthquakes on the North Anatolian Fault: possible signals for preferred earthquake propagation direction , Geophys. J. Int., doi: 10.1111/j.1365-246X.2008.03709.x.

Falsaperla, S., Cara, F., Rovelli, A., Neri, M., Behncke, B. & Acocella, V., 2010. Effects of the 1989 fracture system in the dynamics of the upper SE flank of Etna revealed by volcanic tremor data: The missing link?, *J. Geophys. Res.*, **115**, B11306, doi:10.1029/2010JB007529.

Graymer, R.W., Ponce, D.A., Jachens, R.C., Simpson, R.W., Phelps, G.A. & Wentworth C.M., 2005. Three-dimensional geologic map of the Hayward fault, northern California: Correlation of rock units with variations in seismicity, creep rate, and fault dip. *Geology*, **33**, 521-524

Graymer, R. W., Sarna-Wojcicki, A. M., Walker, J. P., McLaughlin, R. J. & Fleck, R.J., 2002. Controls on timing and amount of right-lateral offset on the East Bay fault system, San Francisco Bay region, California. *Geol. Soc. Am. Bull.*, **114,** 1471– 1479.

Griffith, A., Sanz, P.F. & Pollard, D., 2009. Influence of Outcrop Scale Fractures on the Effective Stiffness of Fault Damage Zone Rocks. *Pure Appl. Geophys*., **166**,1595–1627

Harding, T.P & Lowell, J.D., 1979. Structural styles, their plate tectonic habitats and hydrocarbon traps in petroleum provinces. *Bull. Am. Ass. Petrol. Geol.*, **63**,1016–1058.

Hobbs, B.E., Means, W.D. & Williams, P.P., 1976. An Outline of Structural Geology, Wiley, New York, N.Y, p. 571.

Improta, L. & Bruno, P. P., 2007. Combining seismic reflection with multifold wide-aperture profiling: An effective strategy for high-resolution shallow imaging of active faults, *Geophys. Res. Lett.*, 34, L20310, doi:10.1029/2007GL031893.

Jaeger, J.C., Cook, N.G.W. & Zimmerman, R.W., 2007. Fundamentals of rock mechanics, 4th ed., 475 pp. Blackwell, Malden, Mass

Jurkevics, A., 1988. Polarization analysis of three component array data, *Bull. Seism. Soc. Am.*, **78**, 1725-1743.

Kanasewich, E.R., 1981. Time sequence analysis in geophysics. University of Alberta press, 477 pp.

Kelson, K. I. & Simpson, G. D., 1995. Late Quaternary deformation of the southern East Bay Hills, Alameda County, CA. *AAPG Bull.*, **79**, 590.

La Rocca, M., D. Galluzzo, G. Saccorotti, S. Tinti, G. B. Cimini & Del Pezzo, E., 2004. Seismic signals associated with landslides and with a tsunami at Stromboli volcano, Italy, *Bull. Seism. Soc. Am.,* **94(5)**, 1850–1867, doi:10.1785/012003238

Lawson, A. C., 1908. The earthquake of 1868 in A. C. Lawson, ed., The California earthquake of April 18, 1906, Report of the State Earthquake Investigation Commission (Volume I), Carnegie Institution of Washington Publication No. **87**, 434-448,.

Li, Y. -G., Ellsworth, W. L., Thurber, C. H., Malin, P. E. & Aki, K, 1997. Observations of fault zone trapped waves, *Bull. Seismol. Soc. Am.*, **87,** 210–221.

Li, Y. -G. & Leary, P. C., 1990. Fault zone trapped seismic waves, *Bull. Seismol. Soc. Am.*, **80**, 1245–1271.

Li, Y. -G., Leary, P. C., Aki, K., & Malin, P., 1990. Seismic trapped modes in the Oroville and San Andreas fault zones. *Science*, **249**, 763– 765, doi:10.1126/science.249.4970.763.

Li, Y. -G. & Vidale, J. E., 1996. Low-velocity fault-zone guided waves: Numerical investigations of trapping efficiency, *Bull. Seismol. Soc. Am.*, **86**, 371–378.

Lienkaemper, J. J., 1992. Map of recently active traces of the Hayward fault, Alameda and Contra Costa Counties, California, scale 1:24,000, U.S. Geol. Surv. Misc. Field Stud. Map MF-2196, 13 p.

Lienkaemper, J. J., Borchardt, G. & Lisowski, M., 1991. Historic creep rate and potential for seismic slip along the Hayward fault, California. *J. Geophys. Res.*, **96**, 18,261-18,283.

Lewis, M. & Ben-Zion, Y., 2010. Diversity of fault zone damage and trapping structures in the Parkfield section of the San Andreas Fault from comprehensive analysis of near fault seismograms, *Geophys. J. Int.*, **183**, 1579-1595, doi: 10.1111/j.1365-246X.2010.04816.x.

Lewis, M. A., Peng, Z., Ben-Zion, Y. & Vernon, F. L., 2005. Shallow seismic trapping structure in the San Jacinto fault zone near Anza, California. *Geophys. J. Int.,* **162**, 867 – 881, doi:10.1111/j.1365-246X. 2005.02684.x.

Mamada, Y., Kuwahara, Y., Ito, H. & Takenaka, H., 2004. Discontinuity of the Mozumi–Sukenobu fault low-velocity zone, central Japan, inferred from 3-D finite-difference simulation of fault zone waves excited by explosive sources. *Tectonophysics*, **378 (3-4)**, 209-222.

Mandl, G., 2000. Faulting in Brittle Rocks. An Introduction to the Mechanics of Tectonic Faults. Springer, 434 pp.

Maschio, L., Ferranti, L. & Burrato, P., 2005. Active extension in Val d'Agri area, Southern Apennines, Italy; implications for the geometry of the seismogenic belt. *Geophys. J. Int*., **162(2)**, 591–609.

Menardi Noguera, A. & Rea, G., 2000. Deep structure of the Campanian-Lucanian Arc (Southern Apennine, Italy). *Tectonophysics*, **324(4)**, 239–265.

Mizuno, T. & Nishigami, K, 2004. Deep structure of the Mozumi-Sukenobu fault, central Japan, estimated from the subsurface array observation of fault zone trapped waves. *Geophys. J. Int.,* **159 (2)**, 622–642.

Nakamura, Y., 1989. A method for dynamic characteristics estimation of subsurface using microtremors on the ground surface, *Quarterly Rept. RTRI, Jpn.,* **30**, 25-33.

Pastori, M., Piccinini, D., Margheriti, L., Improta, L., Valoroso, L., Chiaraluce, L. & Chiarabba, C., 2009. Stress aligned cracks in the upper crust of the Val d'Agri region as revealed by shear wave splitting. *J. Geophys. Res.,* **179**, 601–614

Peng, Z. & Ben-Zion, Y., 2005. Spatiotemporal variations of crustal anisotropy from similar events in aftershocks of the 1999 *M*7.4 İzmit and *M*7.1 Düzce, Turkey, earthquake sequences. *Geophys. J. Int,* **160 (3)**, 1027–1043.

Peng, Z. & Ben-Zion, Y., 2006. Temporal Changes of Shallow Seismic Velocity Around the Karadere-Duzce Branch of the North Anatolian Fault and Strong Ground Motion. *Pure Appl. Geophys.,* **163**, 567–600.

Peng, Z., Ben-Zion, Y., Michael, A.J. & Zhu, L., 2003. Quantitative analysis of fault zone waves in the rupture zone of the Landers, 1992, California earthquake: Evidence for a shallow trapping structure. *Geophys. J. Int.,* **155**, 1021–1041.

Pitarka, A., Collins, N., Thio, H.K., Graves, R. & Somerville, P., 2006. Implication of rupture process and site effects in the spatial distribution and amplitude of the near-fault ground motion from the 2004 Parkfield earthquake, *In* Proceedings, SMIP06 Seminar on Utilization of Strong motion Data, California Strong Motion Instrumentation Program, Sacramento, CA, 19-40.

Pischiutta, M., 2010. The polarization of horizontal ground motion: an analysis of possible causes. PhD thesis, Università di Bologna "Alma Mater Studiorum".

Pischiutta, M., Rovelli, A., Fletcher, J.B., Salvini, F. & Ben-Zion, Y., 2010. Study of Ground Motion Polarization in Fault Zones: a Relation with Brittle Deformation Fields? American Geophysical Union, Fall Meeting 2010, abstract #S13A-1960

Provost, A.-S. &. Houston, 2003. Stress orientations in northern and central California: Evidence for the evolution of frictional strength along the San Andreas plate boundary system. *J. Geophys. Res.,* **108(B3)**, 2175, doi:10.1029/2001JB001123.

Riedel, W., 1929. Zur mechanik geologischer Brucherscheinungen. Zentralblatt Mineral Geol Palaont B:354–368.

Rigano, R., Cara, F., Lombardo G. & Rovelli, A., 2008. Evidence of ground motion polarization on fault zones of Mount Etna volcano, *J. Geophys. Res.*, doi:10.1029/2007JB005574.

Rovelli, A., Caserta, A., Marra, F. & Ruggiero, V., 2002. Can seismic waves be trapped inside an inactive fault zone? The case study of Nocera Umbra, central Italy, *Bull. Seism. Soc. Am.*, **92,** 2217-2232.

Salvini, F., Billi, A. & Wise, D.U., 1999. Strike-slip fault-propagation cleavage in carbonate rocks: the Mattinata Fault Zone, Southern Apennines, Italy. *J. Struct. Geol.*, **21**, 1731-1749.

Savage, J. C. & M. Lisowski, 1993. Inferred depth of creep on the Hayward fault, central California. *J. Geophys. Res.*, **98**, 787– 793.

Seeber, L., Armbruster, J. G., Ozer, N., Aktar, M., Baris, A., Okaya, D., Ben-Zion, Y. & Field, E., 2000. The 1999 Earthquake Sequence along the North Anatolia Transform at the Juncture between the Two Main Ruptures, in *The 1999 Izmit and Duzce Earthquakes: preliminary results*, edit. Barka A., O. Kazaci, S. Akyuz and E. Altunel, Istanbul technical university, 209-223.

Spudich P, Hellweg, M. & Lee, H. K., 1996. Directional topographic site response at Tarzana observed in aftershocks of the 1994 Northridge California earthquake: Implications for mainshocks motions, *Bull. Seismol. Soc. Am.*, **86**, 193-208.

Spudich, P. & Olsen, K. B., 2001. Fault zone amplified waves as a possible seismic hazard along the Calaveras Fault in central California, *Geophys. Res. Lett.*, 28(13), 2533–2536, doi:10.1029/2000GL011902.

Spudich, P & Xu, L., 2003. Documentation of software package ISOSYN: Isochrone integration programs for earthquake ground motion calculations, CD accompanying IASPEI *Handbook of Earthquake and Engineering Seismology*, 72 pp.

Storti, F., Salvini, F. & McClay, K., 1997. Fault related folding in sandobox analogue models of thrust wedges. *J. Struct. Geol.*, **19**, 583-602.

Yu, E. & Segall, P., 1996. Slip in the 1868 Hayward earthquake from the analysis of historical triangulation data. *J. Geophys. Res.,* **101**, 16,101–16,118.

Wakabayashi, J., 1999. Distribution of displacement on, and evolution of, a young transform fault system: the northern San Andreas fault system, California. *Tectonics*, **18**, 1245– 1274.

Wakabayashi, J., Hengeshb, J.V. & Sawyerc, T.L., 2004. Four-dimensional transform fault processes: progressive evolution of step-overs and bends. *Tectonophysics*, **392**, 279– 301

Wise, D. U. & Vincent, R. J., 1965. Rotation axis method for detecting conjugate planes in calcite petrofabric. *Am. J. Sci.*, **263**, 289-301.

Williams, P. L., 1992. Geologic record of southern Hayward Fault earthquakes, in Proceedings of the Second Conference on Earthquake Hazards in the Eastern San Francisco Bay Area, edited by G. Borchardt et al.. Spec. *Publ. Calif. Div. Mines Geol.*, **113**, 171– 179.

Williams, R.A., Simpson, R.W., Jachens, R.C., Stephenson, W.J., Odum, J.K. & Ponce, D.A., 2005. Seismic reflection evidence for a northeast-dipping Hayward fault near Fremont, California: Implications for seismic hazard. *J. Geophys. Res.*, **114**, doi:10.1029/2005GL023113.